

Modeling Water Diffusion Anisotropy Within Fixed Newborn Primate Brain Using Bayesian Probability Theory

Christopher D. Kroenke,^{1*} G. Larry Bretthorst,¹ Terrie E. Inder,³ and Jeffrey J. Neil^{1,2}

An active area of research involves optimally modeling brain diffusion MRI data for various applications. In this study Bayesian analysis procedures were used to evaluate three models applied to phase-sensitive diffusion MRI data obtained from formalin-fixed perinatal primate brain tissue: conventional diffusion tensor imaging (DTI), a cumulant expansion, and a family of modified DTI expressions. In the latter two cases the optimum expression was selected from the model family for each voxel in the image. The ability of each model to represent the data was evaluated by comparing the magnitude of the residuals to the thermal noise. Consistent with previous findings from other laboratories, the DTI model poorly represented the experimental data. In contrast, the cumulant expansion and modified DTI expressions were both capable of modeling the data to within the noise using six to eight adjustable parameters per voxel. In these cases the model selection results provided a valuable form of image contrast. The successful modeling procedures differ from the conventional DTI model in that they allow the MRI signal to decay to a positive offset. Intuitively, the positive offset can be thought of as spins that are sufficiently restricted to appear immobile over the sampled range of *b*-values. Magn Reson Med 55:187–197, 2006.

© 2005 Wiley-Liss, Inc.

Key words: MRI; diffusion anisotropy; brain; newborn; Bayesian probability theory

In this study we investigated three mathematical models for analyzing water diffusion within formalin-fixed perinatal primate brain. They were applied with the goal of evaluating the complexity of diffusion MRI data in this experimental system. On the microstructural scale, developing brain tissue varies from region to region, and also evolves with brain maturation. As a result, the diffusion-attenuated MRI signal is expected to reflect these changes through spatial and temporal variations. Methods to analyze diffusion MRI data must be flexible enough to accommodate a diverse array of tissue characteristics, but should encode this flexibility in a simple manner. It is hoped that

a better understanding of the degree of complexity in the MRI data will help elucidate the relationship between cellular level tissue characteristics and diffusion MRI data.

Two of the analysis procedures pursued in this study incorporate flexibility by using Bayesian probability theory to perform model selection calculations. The Bayesian framework provides a convenient way to determine whether statistically significant improvements in agreement between a model expression and the data justify the use of a complex mathematical expression over a simpler one. In previous studies of adult human brain, F-statistic calculations were used to make similar determinations (1–3). In the study described here we further extended this work to determine how completely the selected model expressions represent the data. Following the Bayesian modeling procedures, the residuals between the model predictions and the data are computed. The fidelity of the model expressions to the data is evaluated by comparing the magnitude of the residuals to the magnitude of the noise in regions of the images that are devoid of signal. Regions in which the residuals are larger than the noise are areas that deviate from the model. By determining the minimum number of parameters needed to model the data to within the noise, the model selection calculations reveal the minimum/optimal number of parameters within each class necessary to model the data to within the noise.

Diffusion MRI has much clinical potential for monitoring cerebral development in prematurely delivered human infants (4). We chose fixed baboon brain as the focus of this study for two reasons: First, it has high clinical relevance for both normal development and brain injury in humans (5,6). Second, it is possible to employ very long MR scanning times with fixed tissue. This allows data to be acquired with a very high signal-to-noise ratio (SNR), spatial resolution, and diffusion angular and radial resolution. Further, it has been demonstrated in rodent models that diffusion anisotropy characteristics are well preserved in fixed tissue (7,8).

A number of mathematical expressions have been used to model brain diffusion MRI data. The most commonly used approach that incorporates directionally-dependent diffusivity is the conventional diffusion tensor imaging (DTI) model (1,9). According to the conventional DTI formalism, diffusion is characterized by three unique diffusion coefficients in directions parallel to local *x*-, *y*-, and *z*-axes. Diffusion in oblique directions is characterized by a linear combination of the three on-axis diffusivities. The conventional DTI model parameters clearly reveal cellular-level anatomy in myelinated white matter (10) and developing cortical gray matter (4).

More elaborate models of diffusion MRI data have also been proposed. Some of these models were motivated by

¹Department of Radiology, St. Louis, Missouri, USA.

²Department of Pediatric Neurology, Washington University, St. Louis, Missouri, USA.

³Neonatal Neurology, Royal Women's and Royal Children's Hospital, Murdoch Children's Research Institute, Parkville, Australia.

Grant sponsor: NIH; Grant numbers: NS37357; CA83060; NS43010; HL52636 BPD; P51RR13986; Grant sponsors: Murdoch Children's Research Institute; Allen P. and Josephine B. Green Fund for Pediatric Neurology.

*Correspondence to: Christopher D. Kroenke, Ph.D., Biomedical MR Laboratory, Campus Box 8227, Washington University School of Medicine, 2313 East Building, 4525 Scott Ave., St. Louis, MO 63110.

E-mail: kroenke@wustl.edu

Received 23 December 2004; revised 18 August 2005; accepted 18 August 2005.

DOI 10.1002/mrm.20728

Published online 8 December 2005 in Wiley InterScience (www.interscience.wiley.com).

© 2005 Wiley-Liss, Inc.

observations that diffusion is not accurately characterized simply by a single diffusion coefficient along a given direction. Specifically, at higher b -values the MRI signal attenuation curve is non-monoexponential with b . To address these observations, both multiexponential models (11–13) and high-order generalizations of the diffusion tensor (14–16) have been proposed. In addition, models have been formulated to parameterize heterogeneous collections of fiber tract orientations within a single voxel. These models include a sum of multiple diffusion tensors (12,13), a spherical harmonic decomposition of the diffusion MRI signal (3,17,18), and explicit models of multiple fiber orientations (11). Our goal was to generate an analysis procedure that would retain the simplicity and clear relationship to microstructure present in the conventional DTI model, but would also include elaborations on the conventional DTI model when appropriate.

The three models/model classes investigated in this study were the conventional DTI model, a cumulant expansion of the diffusion MRI signal, and a modified family of DTI models. The conventional DTI model consists of a single expression, whereas the latter two consist of multiple expressions. To gauge the abilities of these three strategies to account for the diffusion MRI data, the residuals are compared with the noise. Under ideal circumstances, the standard deviation (SD) in the residuals equals the SD in the noise, indicating that the model accounts for all of the data while it minimizes the susceptibility of parameter estimations to differences in noise characteristics between data sets. A comparison of the residuals with the noise following conventional DTI analysis leads to the identification of specific regions in the brain where discrepancies between the conventional DTI model and MRI data are most severe. The latter two investigated model classes proved to be capable of accounting for the data to within the noise. Further, within these classes the number of parameters needed to accurately model the data (determined using probability theory) varies regionally in a manner that is related to the underlying brain microstructure.

The cumulant expansion and the modified family of DTI expressions both differ from the conventional DTI model in two primary ways: First, the two model classes enable tuning of the number of adjustable parameters to each individual voxel. Although the two model classes parameterize the data in different ways, both procedures identify expressions that model the data to within the noise using six to eight adjustable parameters per voxel. Second, both model classes allow the data to be modeled as decaying to either a positive offset or to zero with increased diffusion weighting, whereas the conventional DTI model assumes that the data decay to zero. Model selection calculations reveal that the inclusion of an offset parameter effectively parameterizes the previously described high b -value deviation from the DTI model. The offset parameter exhibits contrast similar to that described for the “slow component” of biexponential analysis (12,13), being larger in myelinated white matter than in gray matter, yet the modified DTI model has fewer adjustable parameters than previously proposed non-monoexponential models of diffusion anisotropy. Interestingly, the magnitude of the offset parameter appears to increase in association with myelin formation.

The cumulant expansion and modified DTI model classes applied in this study are derived and assessed in a phenomenological manner. They are chosen simply because they accurately account for the experimental data, not because the model parameters necessarily directly correspond to physical characteristics of tissue structure. However, the conclusions drawn from this procedure are general. The results suggest that only six to eight adjustable parameters are necessary to account for the diffusion MRI data to within the noise. Models with a greater number of adjustable parameters are not warranted by the data. Further, though the signal decay vs. b -value along a given direction is clearly non-monoexponential, the addition of a constant term is sufficient to account for this deviation from a monoexponential function without the need to include a second exponential decay term (a biexponential model). Finally, the data from roughly one-third of voxels within the brain can be accounted for with the use of six parameters. The voxels that require more than six parameters are mainly present in the white matter, possibly reflecting the complexity of crossing, myelinated fibers. Since this study was confined to the immature developing brain, which is not yet fully myelinated, it is possible that white matter of adult brain has a higher proportion of voxels that require models with high-order terms.

MATERIALS AND METHODS

Bayesian Calculations and Markov Chain Monte Carlo (MCMC) Simulations

Bayesian probability theory provides a framework for determining the “posterior probability” for model parameters over specified ranges given a model expression and data (19). A robust numerical method for implementing Bayesian calculations utilizes MCMC simulations (20,21). Bayesian/MCMC procedures were previously described for estimating parameters of the conventional DTI model from diffusion MRI data (22).

The calculations presented here extend the Bayesian/MCMC approach (22) to simultaneously estimate the posterior probability of diffusion anisotropy model parameters and compare the relative probabilities of various model expressions against each other. The latter part of the calculation is referred to as “model selection.” Model selection is a simple conceptual extension of parameter estimation whereby a model parameter is assigned as an index that specifies which expression from a set is used to represent the data (23,24). The posterior probability for this index therefore indicates the relative probabilities of the model expressions.

Three calculations were performed. All three cases utilized MCMC simulations to approximate the posterior probabilities of the relevant model parameters. For the latter two model classes, MCMC simulations were also used to perform model selections. In each case the model expressions were applied independently to each voxel in the image. The conventional and modified DTI calculations utilized 50 Markov chain simulations, each of which involved 50 sampling steps, for each voxel. The number of simulations and sampling steps was 32 and 32, respectively, for the cumulant expansion calculations. Computa-

tions implementing the conventional and modified DTI models were performed in parallel, using 32 Intel Itanium 2 processors. These calculations required approximately 1 hr per 128×128 voxel image.

Conventional DTI Model

The conventional DTI model is defined as (1,9):

$$S(\vec{q})/S(0) = \exp(-\Delta\vec{q} \cdot D \cdot \vec{q}^T) \quad [1a]$$

in which D is a symmetric 3×3 matrix containing three real and positive eigenvalues

$$D = \begin{pmatrix} D_{xx} & D_{xy} & D_{xz} \\ D_{xy} & D_{yy} & D_{yz} \\ D_{xz} & D_{yz} & D_{zz} \end{pmatrix} \\ = R(\phi, \theta, \psi) \cdot \begin{pmatrix} \lambda_1 & 0 & 0 \\ 0 & \lambda_2 & 0 \\ 0 & 0 & \lambda_3 \end{pmatrix} \cdot R^T(\phi, \theta, \psi), \quad [1b]$$

\vec{q} is defined in Eq. [4], $S(0)$ is the signal amplitude for $\vec{q} = (0,0,0)$, and $R(\phi,\theta,\psi)$ is a 3×3 rotation matrix that relates the laboratory frame to the voxel-specific diffusion tensor frame. Bayesian calculations were performed to estimate $S(0)$ and the six elements of the diffusion tensor (seven adjustable parameters total) as described by Behrens et al. (22).

Cumulant Expansion Model Class

A cumulant expansion (see Appendix C in Ref. 19) plus an offset, C , is an adaptable class of expressions. Therefore, it was used to explore the nature of the observed deviations in the data from the DTI model (described in Results). The resulting expression is

$$\frac{S(\vec{q})}{S(0)} = \exp\left(\Delta \sum_i \sum_j \sum_k (\sqrt{-1})^{i+j+k} (q_x)^i (q_y)^j (q_z)^k E_{ijk}\right) + C. \quad [2]$$

In contrast to the conventional DTI model, a voxel-specific ‘‘principal’’ frame cannot be uniquely defined for Eq. [2]. Therefore the subscripts x , y , and z refer to the laboratory frame. The E_{ijk} are coefficients for moments of order $i + j + k$. The coefficients of order 2 correspond exactly to the six elements of the diffusion tensor, and coefficients of order 4 represent diffusional kurtosis terms (14). Higher-order moments were previously interpreted in terms of a generalized diffusion equation by Liu et al. (15). The positive offset term, C , corresponds to the fraction of the signal for which decay is too slow to quantify. In the cumulant expansion calculation, the set of E_{ijk} necessary to model the data is expected to vary from voxel to voxel. Therefore, both the parameter set and the parameter values must be estimated for each voxel. This calculation is described in detail in the Appendix.

Modified DTI Model Class

The final class of models applied to the data was motivated by the observation that for each voxel, a relatively simple cumulant expansion can model the MRI data to within the noise (see Results). Bayesian model selection was employed to determine the most appropriate of the following expressions to model the data for each voxel:

$$S(\vec{q})/S(0) = \begin{cases} DTI + C \\ DTI \\ Prolate + C \\ Prolate \\ Oblate + C \\ Oblate \\ Isotropic + C \\ Isotropic \\ C \\ 0 \end{cases}. \quad [3]$$

where DTI refers to the expression in Eq. [1a], and C is an offset term as in Eq. [2]. The terms ‘‘prolate,’’ ‘‘oblate,’’ and ‘‘isotropic’’ are simplifications of the DTI model that allow for axial (prolate, oblate) or radial (isotropic) symmetry. Strictly speaking, Prolate is defined by constraining Eq. [1b] so that $\lambda_1 = \lambda_2 < \lambda_3$ and $\psi = 0$; Oblate is defined by constraining $\lambda_1 < \lambda_2 = \lambda_3$ and $\psi = 0$; and Isotropic is defined by constraining $\lambda_1 = \lambda_2 = \lambda_3$ and $\theta = \phi = \psi = 0$. The resulting number of adjustable parameters within the terms DTI, prolate, oblate, and isotropic are 7, 5, 5, and 2, respectively. The details of the Bayesian model selection calculation using Eq. [3] have been published elsewhere (23).

Data Acquisition

An immersion fixed (10% formalin) brain from a baboon infant was obtained from the Southwest Foundation for Biomedical Research, San Antonio, TX. The baboon was euthanized, following American Association for Accreditation of Laboratory Animal Care guidelines, 2 days after it was delivered naturally at full term (185 days gestation). For diffusion MRI analysis, the brain was placed within a small container of 10% formalin, and experiments were performed at ambient magnet bore temperature (18°C). The formalin container/brain was inserted into a 7 cm inner diameter (i.d.) linearly polarized Litz RF coil (Doty Scientific, Columbia, SC). The coil was tuned to 201.5 MHz and matched to 50 Ω impedance. The RF coil was placed within a 10-cm i.d., three-axis gradient coil system (Magnex Scientific, Oxford, UK) that is capable of producing magnetic field gradients of up to 60 G/cm. The gradient coils reside in a 4.7 T magnet (Oxford Instruments, Oxford, UK) that is controlled by a Varian (Palo Alto, CA) INOVA console.

Diffusion-weighted images were generated using a standard 2D spin-echo imaging (single acquisition per RF excitation) pulse sequence. The image of a 0.5-mm-thick slice was acquired coronally with an in-plane resolution of 0.5×0.5 mm. The field of view (FOV) and number of points acquired were respectively 4.8 cm and 96 in the phase-encode dimension, and 6.4 and 128 in the frequency-encode dimension. The image acquisition parameters were TR =

Table 1
Diffusion-Sensitization Gradient Settings

G_α (G/cm)	G_β (G/cm)	G_γ (G/cm)	b (ms/ μm^2)
0	0	0	0
0	2.5	2.5	0.11
7.6	0	0	0.50
5.1	7.6	2.5	0.78
0	0	10.1	0.89
2.5	5.1	10.1	1.17
0	12.7	0	1.39
5.1	0	12.7	1.60
7.6	2.5	12.7	1.94
17.7	10.1	0	3.60
2.5	20.3	5.0	3.83
20.3	2.5	5.1	3.83
10.1	7.6	17.7	4.10
2.5	5.1	22.8	4.77
12.7	17.7	15.2	6.10
25.3	7.6	7.6	6.55
7.6	10.1	25.3	6.94
27.9	0	10.1	7.60
5.1	27.9	10.1	7.83
20.3	0	22.8	8.05
22.8	15.2	17.7	9.21
7.6	32.9	0	9.88
30.4	12.7	15.2	11.38
30.4	20.3	12.7	12.93
17.7	12.7	35.5	14.98
35.5	17.7	15.2	15.59
38.0	32.9	10.1	22.75

2.3 s, TE = 67 ms, and number of averages = 4. Diffusion sensitization was incorporated into the spin-echo sequence according to the Stejskal-Tanner scheme (25), with gradient length $\delta = 5$ ms, gradient spacing $\Delta = 50$ ms, and strength along the x , y , and z components varying from 0 to 38 G/cm. Diffusion anisotropy was measured by acquiring 162 images while varying the relative strength and polarity of the diffusion-sensitization gradients along the x -, y -, and z -axes of the laboratory frame. The diffusion sensitization sampling scheme contains both a random component, to minimize sensitivity to systematic errors, and a regular component, to ensure a uniform sampling of \vec{q} value directions. The 162 images consist of six iterations of 27 randomly chosen gradient settings. Table 1 lists the 27 settings along axes α , β , and γ . The six iterations were performed with (α, β, γ) corresponding to (x, y, z) , (y, z, x) , (z, x, y) , $(x, y, -z)$, $(-y, z, x)$, and $(z, -x, y)$, respectively, to yield six repetitions of the setting $(0, 0, 0)$ and 156 additional unique gradient configurations (157 unique directions total). Here diffusion sensitization strength is quantified in terms of the induced spatial frequency in magnetization phase, q_α (26):

$$q_\alpha = \gamma G_\alpha \delta / (2\pi) \quad [4]$$

where γ is the ^1H magnetogyric ratio, α specifies the direction of the diffusion-sensitization gradients (x , y , z , or some oblique combination), and G_α is the magnitude of the diffusion-sensitization gradient pulse, which is a vector quantity $\vec{G} = (G_x, G_y, G_z)$. The total scan time for this procedure was 42 hr, and the SNR for the $S(0)$ data points within brain was approximately 30.

In the diffusion MRI analysis, the signal amplitude for a single voxel, S , was recorded for varying settings of the vector $\vec{q} = (q_x, q_y, q_z)$, to obtain the diffusion decay curve $S(\vec{q})$. To obtain the signal amplitudes, phase-sensitive images were calculated from the complex k -space data using methods previously described in velocity imaging studies (27). For each 2D image, three phase parameters were found that rendered the data purely absorptive (i.e., the “imaginary” channel images were purely white noise). These three parameters correspond to one frequency-independent phase and two linear frequency-dependent corrections (one for the phase-encode direction and one for the frequency-encode direction). From these procedures, one $S(\vec{q})$ curve, consisting of 162 data values, was extracted from each voxel in the image.

RESULTS

Conventional DTI Analysis

Figure 1a shows a T_2 -weighted coronal spin-echo image of a formalin-fixed baboon brain. The image was acquired with the diffusion-sensitizing gradients set to zero amplitude, $\vec{q} = (0, 0, 0)$. For this study, six such images and 156 additional images with differing nonzero directions and magnitudes of \vec{q} were acquired. Figure 1b displays a plot of the signal intensity, $S(\vec{q})$, for a single voxel vs. the magnitude of \vec{q} . As expected, the general trend for $S(\vec{q})$ is to decay with increasing $|\vec{q}|$. Note that diffusion anisotropy contributes to the variation in $S(\vec{q})$ for each value of $|\vec{q}|$, since measurements were made at several directions for each value of $|\vec{q}|$.

The data from each voxel in Fig. 1a were analyzed using the conventional DTI model (Eq. [1]). To assess the fidelity of this model to the data, $S(\vec{q})$ values were back-calculated from the conventional DTI parameter values that maximize the posterior probability. These back-calculated values, $S^{model}(\vec{q})$, were then compared with the experimentally observed values, $S^{observed}(\vec{q})$. Figure 1c shows the residuals ($S^{model}(\vec{q}) - S^{observed}(\vec{q})$) from the Fig. 1b data. The residuals are not randomly distributed but display a systematic positive-negative-positive pattern with increasing $|\vec{q}|$. This systematic pattern contributes to the residuals and arises from the poor fit of the conventional DTI model to the data.

To ascertain how extensive such deviations are throughout the image, the SD in the residuals was calculated for each voxel. Figure 2a is a grayscale image of the SDs in the residuals (hereafter termed the “residual intensity”) following conventional DTI analysis. The specificity of high residual intensity within white matter suggests that the deviations of the DTI model from the data are related to the underlying brain microanatomy. Additionally, high residual intensity is also observed at the brain/formalin and formalin/air interfaces due to partial volume effects.

The dashed line of Fig. 2d is a histogram of residual intensities from voxels in which the directionally-averaged apparent diffusion coefficient (ADC) ranges from 1 to $4.5 \mu\text{m}^2/\text{ms}$. These voxels are located within the brain and exclude voxels located at the brain/formalin interface. For comparison, the distribution of residual intensities from voxels outside of both the brain and formalin has a mean

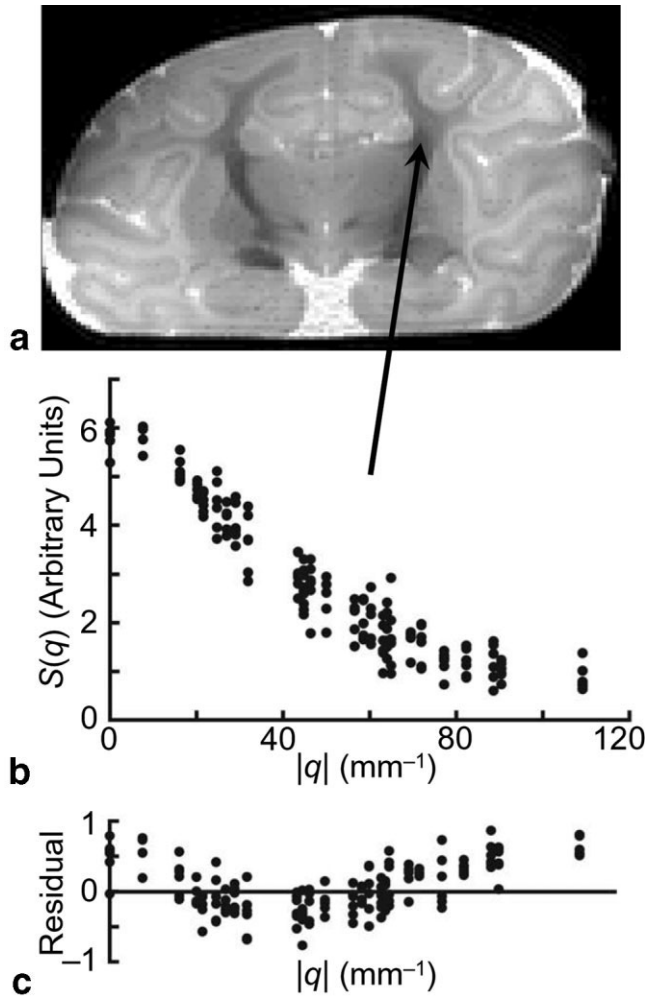


FIG. 1. **a:** T_2 -weighted coronal image of a fixed baboon infant brain. This image was acquired with no diffusion weighting ($\vec{q} = (0,0,0)$). **b:** For the voxel indicated by the arrow, the signal amplitude $S(\vec{q})$, sampled at 162 \vec{q} values, is plotted vs. the magnitude $|\vec{q}|$. **c:** Residual differences between the measured $S(\vec{q})$ and the expected $S(\vec{q})$ obtained from the estimated DTI model parameters. The residual differences demonstrate systematic deviations of the experimental data from the DTI model.

value of 0.26 and SD of 0.034 (represented as the shaded area in Fig. 2d). Consistent with the Fig. 2a image, the distribution of brain voxel residual intensities is significantly larger (i.e., shifted rightward) than the distribution that arises from the noise.

Cumulant Expansion Analysis

To investigate the nature of the diffusion signal deviations from the conventional DTI model, the diffusion MRI data were modeled using a cumulant expansion. Figure 2b is an image of the SDs in the residuals following the cumulant expansion calculation. The dotted line in Fig. 2d is a distribution of Fig. 2b residual intensity values within the same voxels used to generate the distribution of the conventional DTI results. The deviations that give rise to gray/white matter contrast in Fig. 2a are absent in Fig. 2b. Additionally, the cumulant expansion histogram in Fig. 2d

overlaps the random noise distribution represented by the shaded region. Therefore, with the exception of voxels located at the interface between the brain and the surrounding formalin, Eq. [2] successfully models the data to within the noise. (Note that due to partial volume averaging effects, voxels located at the brain/formalin interface contain two well-resolved components consisting of high diffusivity within formalin and low diffusivity within brain. As a result, the signal from these voxels is not well modeled with a single cumulant expansion.)

Results from the cumulant expansion model selections are presented in Fig. 3. Figure 3a is an image of the model type parameter, which is equal to 1 for voxels that contain no signal, 2 for voxels containing a nondecaying signal vs. diffusion weighting, 3 for voxels containing a signal that decays to zero, and 4 for voxels that contain a signal that decays to a positive offset. The model selection procedure assigns values of 1 and 3 to regions that contain air and formalin, respectively. Throughout the brain, the model selection procedure consistently returns a model type of 4, which indicates the MRI signal is more accurately modeled as decaying to a positive offset than to zero. This offset term is the fractional signal from each voxel that can be characterized by an ADC of $1/b_{max}$, or $0.04 \mu\text{m}^2/\text{ms}$.

Figure 3b is an image of the number of cumulant expansion terms in the MCMC simulation that had maximum posterior probability for each voxel. Figure 3c shows a histogram of these results. In most cases the mean number of terms is six to eight. Two of these parameters are $S(0)$ and C , and therefore, on average, four to six independent E_{ijk} parameters are needed in each voxel. White matter voxels require the largest number of cumulant expansion terms, indicating that the diffusion signal in these regions has a more complex structure. A comparison of the four to six selected E_{ijk} parameters with the six D_{ij} of the conventional DTI model reveals that the MRI data may be represented to within the noise without drastically increasing the complexity of the conventional DTI model.

To further compare the cumulant expansion analysis with the DTI model, the MCMC simulations were classified in terms of the expansion orders. Simulations with only second-order terms were classified as order 2, simulations with only second- and fourth-order terms were classified as order 4, and simulations with sixth- or higher-order terms were classified as order 6. Figure 3c is an image of the most probable order (i.e., the order for which the MCMC procedure returned the most simulations) for each voxel. As stated above, the conventional DTI expression corresponds to order 2. Therefore, voxels given values greater than 2 in Fig. 3c signify areas in which there is evidence for high-order deviations. In all of the formalin voxels and 80.5% of the brain voxels the cumulant expansion order is 2. In 19.2% of the brain voxels, the order is 4. In 0.3% of brain voxels, the order is 6. Fourth- and higher-order expressions are observed primarily within white matter structures, such as the corpus callosum, internal capsule, and optic nerve. Within cortical gray matter, second-order expressions are more frequently selected to model the data.

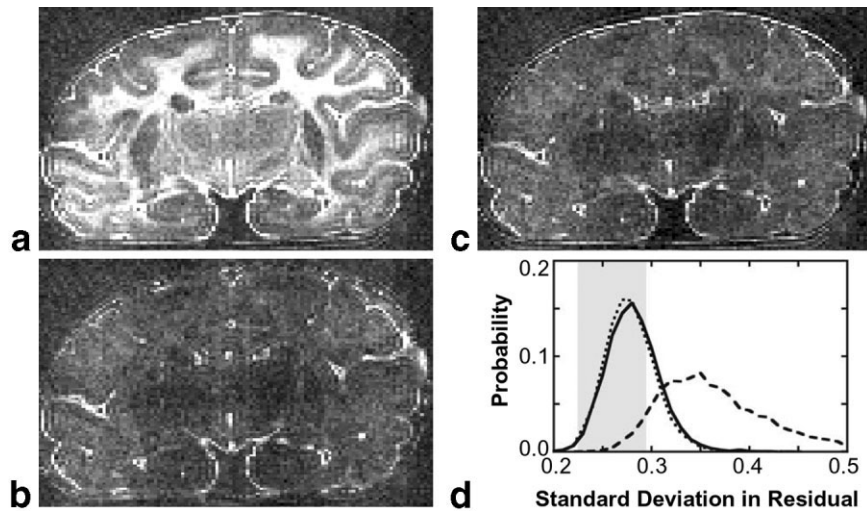


FIG. 2. Images of the SDs in the residuals (the “residual intensity”) from (a) the conventional DTI model (Eq. [1]), (b) the cumulant expansion (Eq. [2]), and (c) the modified DTI analysis (Eq. [3]). Bright pixels indicate large SDs and a poor approximation of the data. The intensity outside the brain shows the SD of the experimental (random thermal) noise. In a, the residual intensity is generally higher within the brain than it is outside, and residual intensity variations correspond to the biological structure. These image features are greatly reduced in b and c, indicating higher fidelity of the latter models to the experimental data. d: Distributions of the SDs in the residuals plotted in images a–c. Dashed, dotted, and solid lines correspond to distributions arising from conventional DTI, cumulant expansion, and modified DTI analyses, respectively. The shaded region is the mean ± 1 SD in the distribution of pixel intensities outside of the brain.

Modified DTI Analysis

The preceding two calculations demonstrate that 1) the data systematically deviate from the DTI model, and 2) the data may be modeled within the noise using a six-to-eight-parameter cumulant expansion, provided that one of the parameters is a positive offset. To assess the importance of high-order terms of the cumulant expansion, a third calculation was performed using the family of modified DTI models given in Eq. [3]. These models allow the MRI signal to decay to a positive offset, but do not contain terms of order greater than 2.

Figure 2c displays the SDs in the residuals from the modified DTI analysis. Similarly to the cumulant expansion analysis, the gray/white matter contrast of Fig. 2a is absent in Fig. 2c. The distribution of Fig. 2c brain voxel residual intensities is plotted as a solid line in Fig. 2d. The modified DTI analysis yields a distribution of residuals that is slightly larger than, but nearly identical to, the cumulant expansion distribution. Through a close comparison of Fig. 2b and c, slightly higher residual intensities may be seen in Fig. 2c within voxels that were modeled using high-order cumulant expansion terms (i.e., the yellow and white voxels in Fig. 3c). These voxels cause the slight rightward shift of the modified DTI residual distribution in Fig. 2d.

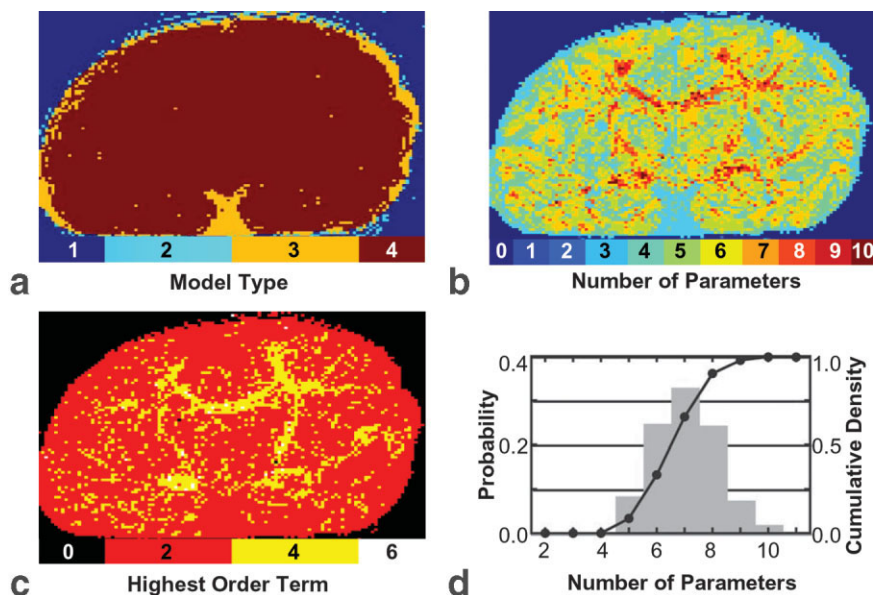
As illustrated in Fig. 4a, the modified DTI expressions represent varying degrees of symmetry in diffusion. The expressions with the maximum posterior probability are shown in Fig. 4b. In 33% of the brain voxels, the most probable model corresponds to oblate (16%) or prolate (17%) symmetry. In these cases the modified DTI calculation utilizes fewer adjustable parameters to model the data than the conventional DTI model. On a coarse level, cortical gray matter is associated with prolate symmetry in diffusion (orange), oblate diffusion is observed in the im-

mediately subcortical white matter (lime green), and the DTI + C expression is observed in the deeper white matter (dark brown). Figure 4c shows orientations obtained from ϕ , θ , and ψ values of color-coded diffusion ellipsoids (28) within the region outlined in Fig. 4b.

Consistent with the cumulant expansion modeling procedure, expressions that contain a positive offset are selected for nearly every voxel within the brain. The value of this parameter, expressed as percent of $S(0)$, is shown in Fig. 5. The offset reaches 15% of the total signal in the posterior limb of the internal capsule. The constant offset is not large in all white matter structures, however, since it is nearly absent in the corpus callosum. The observed contrast in the offset image indicates that regions with large offset terms correlate strongly with myelination at this developmental stage (29).

The inclusion of a constant term and selection of an appropriate number of model parameters are two factors that lead to improved accuracy in the modified DTI parameter estimates relative to the conventional DTI analysis. Figure 6a shows a map of the relative anisotropy (RA) (28) calculated using λ_1 , λ_2 , and λ_3 values estimated from the modified DTI analysis. For comparison with conventional DTI, Fig. 6b shows an image of the difference $RA^{\text{modified}} - RA^{\text{conventional}}$. The difference image is consistently positive within white matter structures, which demonstrates that the increased intervoxel variation in the λ_1 , λ_2 , and λ_3 estimates translates into recovering additional sensitivity to tissue structure. To compare the RA signal with noise ratios from conventional and modified DTI analyses, the ratios $RA/\sigma RA$ were calculated (where σRA is the SD in the RA posterior probability distribution). In regions of the images that are expected to possess significant diffusion anisotropy, the $RA/\sigma RA$ was larger in the modified DTI analysis. For example, the average $RA/\sigma RA$ for the region

FIG. 3. Results from the cumulant expansion modeling procedure. The parameter sets selected for each pixel are displayed in terms of (a) the model type, (b) the expectation value for the number of parameters, and (c) the highest-order E_{ijk} parameter that has a >10% probability of being included in the selected model expression. The distribution of the number of parameters observed within the brain is plotted in d. The probability histogram shows that the data may be modeled to within the noise with only six to eight total parameters for more than 90% of the voxels within the brain.



within the internal capsule indicated in Fig. 6b is 1.6-fold larger in the modified DTI calculations than in the conventional DTI analysis.

DISCUSSION

We used Bayesian probability theory to model the diffusion-attenuated MRI signal within fixed perinatal primate brain tissue. A long data acquisition interval was used to acquire experimental data with high imaging resolution (500 μm -sided cubic voxels), high SNR ($S(0) \approx 30$), and a high degree of angular and radial b -value sampling (162 images and 157 distinct \bar{q} values). For each \bar{q} value, phase-sensitive images were reconstructed, and three calculations were performed using the resulting images as input. First, the conventional DTI model was applied to the data. Subsequently, two model classes (a cumulant expansion and a modified family of DTI models) were applied to the data. In each model application, images were constructed of the SD in the residuals between the model predictions and the experimentally observed data.

Widespread deviations between the experimental data and the conventional DTI model were observed, particularly within white matter. These deviations are attributable to the previously described non-monoexponential behavior of MRI signal decay with increased diffusion sensitization (12,13). The cumulant expansion and modified DTI analyses both proved to be viable methods for modeling the data to within the noise. Within the context of both model classes, we found it necessary to model the MRI

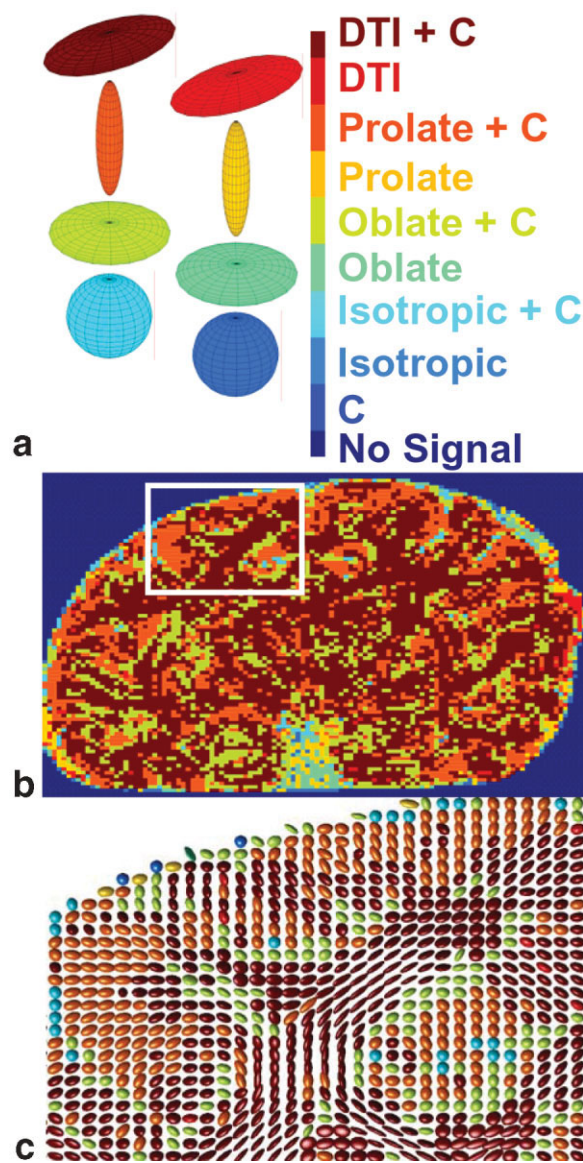


FIG. 4. Model selection results obtained from Eq. [3]. **a:** Diagrams illustrating the symmetry of the various models. For each ellipsoidal surface, the excursion from the center represents the directionally-dependent ADC. **b:** The selected expressions are color-coded, according to the scheme in a, for voxels in the image. **c:** Diffusion ellipsoids are shown oriented according to intravoxel local diffusion frame orientations, which are specified by the angles ϕ , θ , and ψ .

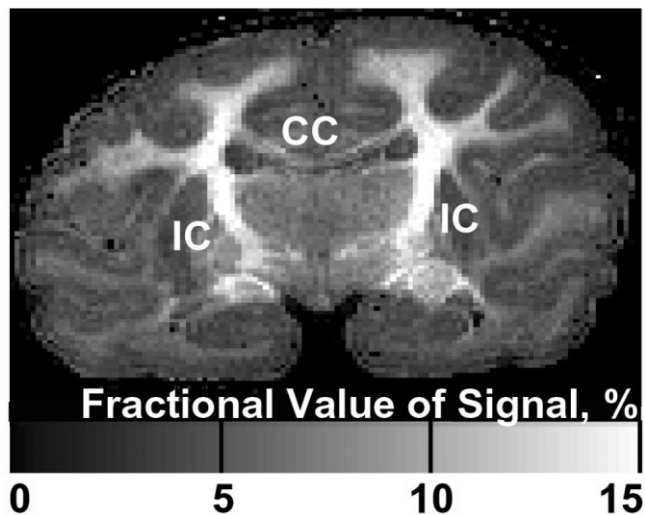


FIG. 5. The fraction of the signal amplitude represented by the offset parameter. The corpus callosum (CC) and internal capsule (IC) are labeled.

signal as decaying to a positive offset to account for the non-monoexponential departure from the conventional DTI model.

Comparison of the Cumulant Expansion With the Modified DTI Analysis

The cumulant expansion and modified DTI analyses are both flexible enough to tune the complexity of the model to the data on a voxel-by-voxel basis. Both strategies allow the data to be fit with a positive offset, but they differ in modeling the decaying component of the MRI signal. The cumulant expansion analysis may extend to high-order terms, whereas the modified DTI analysis is restricted to terms of second order. Though the higher-order expression provides for greater flexibility, a unique principle-axis system cannot be defined for the expressions of order greater than 2. Since the definition of a voxel-specific principal axis system is integral to many fiber-tracking algorithms (30,31), this presents a significant practical advantage in modeling diffusion anisotropy using a second-order expression.

Despite the added potential flexibility of the cumulant expansion, the modified DTI analysis yields a highly similar distribution of residuals within brain voxels (compare solid vs. dotted lines in Fig. 2d). Voxels that exhibit high-order structure (i.e., yellow or white voxels in Fig. 3c) are the most likely to be poorly fit by the modified DTI expressions. Therefore, these voxels were investigated further by calculating the ratios of Fig. 2c to Fig. 2b residual intensities for each yellow or white voxel in Fig. 3c. The distribution of the resulting ratios was found to possess a mean value of 1.05 and an SD of 0.05 (data not shown). Thus, even within voxels specifically identified by the Bayesian model selection algorithm as possessing significant fourth-order or greater terms, these terms have only small effects on the quality of agreement between the data and the model.

The voxels that do exhibit a high-order diffusion structure occur in a nonrandom pattern in the brain. The yellow and white voxels in Fig. 3c cluster within the internal capsule, corpus callosum, and optic nerve. Given the early stage of myelination for most white matter structures at term, high-order terms probably are not as readily observed within perinatal brains as compared to adult. Future efforts to understand the source of this high-order diffusion structure will require the use of data with higher SNR, acquisition schemes that are more sensitive to high-order terms (32), or extrapolation from findings within adult brain (3,12,13,17,33,34).

Comparison of the Modified DTI Model With Other Proposed Models

Other alternatives to the DTI model have been proposed in studies of diffusion within brain tissue. These include a

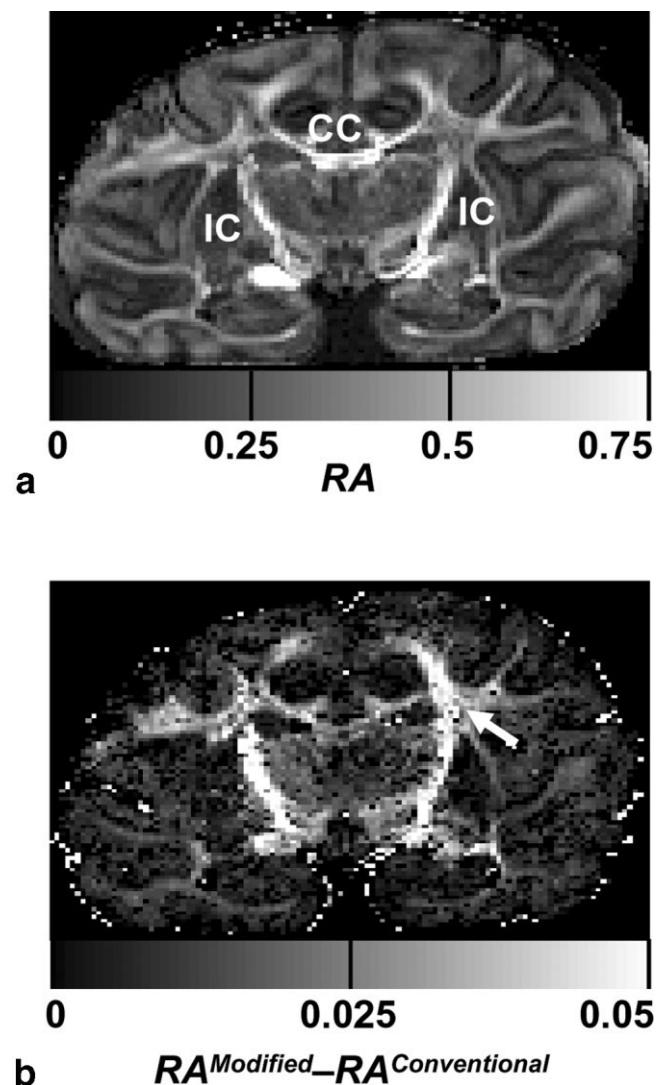


FIG. 6. **a:** RA calculated from Eq. [3]. Improvements in the λ_1 , λ_2 , and λ_3 estimates using Eq. [3] relative to Eq. [1] results in increased ability to detect white matter fibers. **b:** Difference in RA values obtained from Eqs. [1] and [3]. Within the white matter region indicated by the arrow, the SNR of the RA estimates is 1.6-fold larger in the modified DTI analysis than it is in the conventional DTI analysis (see text for details).

sum of diffusion tensors (12,13), a spherical harmonic decomposition (3,17,18), various forms of a cumulant expansion (also termed “generalized DTI”) (14–16), and multicompartamental models (11,35). All of these proposed models require a much greater number of adjustable parameters compared to conventional DTI. In only a small subset of these studies (3,13), χ^2 comparisons or F-statistical tests were used to determine which additional parameters lead to statistically significant improvements in the fit between the model and the data. Further, even in these cases, it is unknown whether the data are modeled to within the noise. The calculation of phase-sensitive images facilitates a direct comparison of the SD in the residuals to the SD in the noise. Such comparisons are more difficult to perform using magnitude images, and therefore have not been explicitly made in the past.

The cumulant expansion and modified DTI analyses demonstrate that the MRI data may be modeled to within the noise using only six to eight adjustable parameters, provided that the data are modeled as decaying to a positive offset. In comparison, models consisting of two independent diffusion tensors (12,13), a spherical harmonic expansion to fourth rank (3,17,18), or a generalized diffusion tensor of order 4 (14–16), require 14, 22, and 22 adjustable parameters, respectively. The cumulant expansion calculation performed here indicates that some high-order terms provide significant improvements in the model for a minority of voxels. However, the inclusion of all high-order terms within the previously described models is not appropriate for our purposes because it would result in overfitting the data. One undesirable consequence of overfitting experimental data is that noise is incorporated into the parameter estimates. Figure 6b demonstrates the increased sensitivity to diffusion anisotropy that is realized when a model that is matched in complexity to the data is used.

Biophysical Interpretation of the Positive Offset

The primary discrepancy between the conventional DTI model and the experimental data stems from the conventional DTI model prediction that $S(\vec{q})$ decays to zero with increasing $|\vec{q}|$, whereas a model that decays to a positive offset more accurately approximates the data. Theoretical studies have shown that a diversity of diffusion barrier structures manifest as a deviation in the MRI signal decay from a monoexponential dependence on the b -value (36–38). With the modified DTI model, we found a phenomenological way to parameterize these manifestations of restricted diffusion as the sum of an apparent diffusion tensor plus a term corresponding to spins that appear immobile over the achieved range of b -values. The absolute size of the offset term depends upon the maximum b -value sampled (with the achieved SNR, it is impossible to distinguish a true constant offset from a decay rate smaller than approximately $1/b_{max}$). For example, offset parameters estimated from a truncated data set, in which the largest 81 b -values are omitted, are on average twofold larger than estimates shown in Fig. 5 (data not shown). Despite the difference in parameter values, the modified DTI model faithfully accounts for the data over both b -value ranges.

The Fig. 5 image clearly indicates that the offset parameter conveys unique biological information that is relevant for primate brain development. Regions within white matter that contain large offset terms were previously found to exhibit a large “slowly diffusing component” in multiexponential analyses (12,13). Offset parameter maps obtained from calculations using a reduced number of b -values and directions retains the major features of the Fig. 5 image, despite the above-mentioned dependence of the offset term upon b_{max} . The large values observed in the posterior limb of the internal capsule (a myelinated structure at term (29)), and lower values within the corpus callosum (unmyelinated at term (29)) suggest that the constant is correlated with some aspect of the myelination process. Observations in brains at other gestational stages further support a connection between the myelination process and the offset parameter (39). The offset term is also consistently observed within the cerebral cortex, albeit at lower levels than that for white matter, which supports previous findings that diffusion within gray matter also deviates from the assumptions of the DTI model (33).

Recently Jensen et al. (14) interpreted deviations in diffusion MRI data from the DTI model in terms of significant kurtosis in the molecular displacement propagator. The diffusional kurtosis imaging (DKI) maps obtained in that study from an adult human also resemble the offset value map shown in Fig. 5, in that large values are observed within myelinated white matter, and smaller but nonzero values are present in the cerebral cortex. The DKI method and the modified DTI model share the common purpose of modeling the non-monoexponential decay of the MRI signal vs. b -value. However, the single offset term of Eq. [3] is a markedly simpler modification than the 15 additional parameters required to incorporate the directional information of diffusional kurtosis (14). From an “Occam’s razor” viewpoint, the modified DTI model is more desirable because of its simplicity.

The calculation of phase-sensitive (as opposed to magnitude) diffusion-weighted images (27) to produce the $S(\vec{q})$ data values greatly facilitated the offset parameter estimates. This is because the noise floor of phase-sensitive images has a mean value of zero and is Gaussian-distributed. In magnitude images, the noise floor is positive and Rician-distributed (40). In principle, Rician noise models (41) can be used to estimate the constant offset term when phase-sensitive images are not available. However, theoretical studies have led to the conclusion that more precise amplitude estimates can be obtained from complex-valued data than from magnitude data (41).

CONCLUSIONS

Using a phenomenological approach, we have identified a concise model that faithfully describes diffusion MRI data with only six to eight adjustable parameters. This finding complements efforts to develop biophysical models of diffusion within brain tissue (11,35,38). Given the known intricacies of brain tissue microstructure, a virtually unlimited number of structural parameters (such as the size and orientation of multiple fiber tracts within a voxel) and dynamic parameters (such as diffusion coefficients in intra- and extracellular environments and exchange between

these compartments) could be conceived in a comprehensive model of water diffusion. The results of this study indicate that for the case of fixed primate brain during gestational development, the complexity of the diffusion MRI data warrants the use of biophysical models with no more than eight adjustable parameters.

ACKNOWLEDGMENT

We thank J.J.H. Ackerman for many helpful discussions throughout the course of these studies.

APPENDIX

Using Eq. [2] to Model Diffusion

To simplify the Eq. [2] calculations, the model expression was tailored for the specific purpose of analyzing diffusion MRI data. As described by Callaghan (26), the diffusion MRI signal, $S(\vec{q})$, is the Fourier transform of the mean displacement probability, $\langle P(r, \Delta) \rangle$. By virtue of being a probability, $\langle P(r, \Delta) \rangle$ must be a real-valued function, which implies that its Fourier transform has an even, real component and an odd, imaginary component:

$$\operatorname{Re}\{S(\vec{q})\} = \operatorname{Re}\{S(-\vec{q})\} \quad \operatorname{Im}\{S(\vec{q})\} = -\operatorname{Im}\{S(-\vec{q})\}. \quad [\text{A.1}]$$

As mentioned in Materials and Methods, inspection of the imaginary components of the phase-sensitive images revealed that they contained only noise. Incorporating the symmetry considerations of Eq. [A.1] and the experimental finding that the measured $S(\vec{q})$ are real-valued, it follows that the only terms necessary in Eq. [2] are those in which $i + j + k$ is even.

Bayesian probability theory was used to analyze the 162 different diffusion-weighted images on a pixel-by-pixel basis using the cumulant expansion. A Metropolis-Hastings MCMC simulation with simulated annealing was used to draw samples from the joint posterior probability for all of the parameters appearing in Eq. [2]. These parameters included the model type (no signal, constant, cumulant expansion without a constant, and cumulant expansion with a constant), the number of expansion terms, the order of each expansion term (the i , j , and k), the cumulant coefficients (the E_{ijk}), and finally the amplitude and magnitude of the constant (if present). To sample this posterior distribution, four basic types of steps were used within the Markov chain: 1) the model type was changed using a uniform proposal; 2) the number of expansion coefficients was either increased or decreased by one using a uniform proposal; 3) the i , j , and k of each cumulant coefficient were increased or decreased using a uniform proposal in such a way that $i + j + k$ was even; and finally 4) the E_{ijk} , $S(0)$, and C were simulated using Gaussian proposals. In steps 1–3, after one of the discrete variables was changed, it was necessary to simulate the E_{ijk} , $S(0)$, and C until the simulation reached equilibrium at a given value of the annealing parameter before a proposed model change was accepted or rejected. Multiple MCMC simulations were run in parallel. The annealing parameter was varied from zero to one in uniform steps. After the annealing parameter reached one, multiple independent samples from each

simulation were saved and used to compute the marginal posterior probability for the various outputs. The cumulant expansion figures shown throughout this paper were generated from these samples by computing the average, SD, and peak parameter values.

REFERENCES

1. Basser PJ, Mattiello J, LeBihan D. Estimation of the effective self-diffusion tensor from the NMR spin echo. *J Magn Reson B* 1994;103:247–254.
2. Basser PJ, Jones DK. Diffusion-tensor MRI: theory, experimental design and data analysis—a technical review. *NMR Biomed* 2002;15:456–467.
3. Alexander DC, Barker GJ, Arridge SR. Detection and modeling of non-Gaussian apparent diffusion coefficient profiles in human brain data. *Magn Reson Med* 2002;48:331–340.
4. Neil JJ, Shiran SI, McKinstry RC, Scheffl GL, Snyder AZ, Almlı CR, Akbudak E, Aaronovitz JA, Miller JP, Lee BCP, Conturo TE. Normal brain in human newborns: apparent diffusion coefficient and diffusion anisotropy measured using diffusion tensor imaging. *Radiology* 1998;209:57–66.
5. Inder TE, Neil JJ, Yoder B, Rees S. Non-human primate models of neonatal brain injury. *Semin Perinatol* 2004;28:396–404.
6. Dieni S, Inder TE, Yoder B, Briscoe T, Camm E, Egan G, Denton D, Rees S. The pattern of cerebral injury in a primate model of preterm birth and neonatal intensive care. *J Neuropathol Exp Neurol* 2004;63:1297–1309.
7. Sun SW, Neil JJ, Liang H-F, He YY, Schmidt RE, Hsu CY, Song SK. Formalin fixation alters water diffusion coefficient magnitude but not anisotropy in infarcted brain. *Magn Reson Med* 2005;53:1447–1451.
8. Sun SW, Neil JJ, Song SK. Relative indices of water diffusion anisotropy are equivalent in live and formalin-fixed mouse brains. *Magn Reson Med* 2003;50:743–748.
9. Basser PJ, Mattiello J, Le Bihan D. MR diffusion tensor spectroscopy and imaging. *Biophys J* 1994;66:259–267.
10. Le Bihan D. Looking into the functional architecture of the brain with diffusion MRI. *Nat Rev* 2003;4:469–480.
11. Assaf Y, Freidlin RZ, Rohde GK, Basser PJ. New modeling and experimental framework to characterize hindered and restricted water diffusion in brain white matter. *Magn Reson Med* 2004;52:965–978.
12. Clark CA, Hedehus M, Moseley ME. In vivo mapping of the fast and slow diffusion tensors in human brain. *Magn Reson Med* 2002;47:623–628.
13. Maier SE, Vajapeyam S, Mamata H, Westin C-F, Jolesz FA, Mulkern RV. Biexponential diffusion tensor analysis of human brain diffusion data. *Magn Reson Med* 2004;51:321–330.
14. Jensen JH, Helpert JA, Ramani A, Lu H, Kaczynski K. Diffusional kurtosis imaging: the quantification of non-Gaussian water diffusion by means of magnetic resonance imaging. *Magn Reson Med* 2005;53:1432–1440.
15. Liu CL, Bammer R, Acar B, Moseley ME. Characterizing non-Gaussian diffusion by using generalized diffusion tensors. *Magn Reson Med* 2004;51:924–937.
16. Ozarslan E, Mareci TH. Generalized diffusion tensor imaging and analytical relationships between diffusion tensor imaging and high angular resolution diffusion imaging. *Magn Reson Med* 2003;50:955–965.
17. Frank LR. Characterization of anisotropy in high angular resolution diffusion-weighted MRI. *Magn Reson Med* 2002;47:1083–1099.
18. Zhan W, Gu H, Xu S, Silbersweig DA, Stern E, Yang Y. Circular spectrum mapping for intravoxel fiber structures based on high angular resolution apparent diffusion coefficients. *Magn Reson Med* 2003;49:1077–1088.
19. Jaynes ET. Probability theory. Cambridge: Cambridge University Press; 2003.
20. Hastings WK. Monte Carlo sampling methods using Markov chains and their applications. *Biometrika* 1970;57:97–109.
21. Metropolis N, Rosenbluth AW, Rosenbluth MN, Teller AH, Teller E. Equation of state calculations by fast computing machines. *J Chem Phys* 1953;21:1087–1092.
22. Behrens TEJ, Woolrich MW, Jenkinson M, Johansen-Berg H, Nunes RG, Clare S, Matthews PM, Brady JM, Smith SM. Characterization and propagation of uncertainty in diffusion-weighted MR imaging. *Magn Reson Med* 2003;50:1077–1088.

23. Bretthorst GL, Kroenke CD, Neil JJ. Characterizing water diffusion in fixed baboon brain. In: Dose V, editor. Bayesian inference and maximum entropy methods in science and engineering. Garching, Germany: American Institute of Physics; 2004. p 1–13.
24. Goggans PM, Chi Y. Using thermodynamic integration to calculate the posterior probability in Bayesian model selection problems. In: Erickson G, Zhai Y, editors. Bayesian inference and maximum entropy methods in science and engineering. Jackson Hole, WY: American Institute of Physics; 2003.
25. Stejskal EO. Use of spin echoes in a pulsed magnetic-field gradient to study anisotropic, restricted diffusion and flow. *J Chem Phys* 1965;43:3597–3603.
26. Callaghan PT. Principles of magnetic resonance microscopy. Oxford, UK: Oxford Science Publications; 1991.
27. Callaghan PT, Xia Y. Velocity and diffusion imaging in dynamic NMR microscopy. *J Magn Reson* 1991;91:326–352.
28. Basser PJ, Pierpaoli C. Microstructural and physiological features of tissues elucidated by quantitative-diffusion-tensor MRI. *J Magn Reson Ser B* 1996;111:209–219.
29. Kinney HC, Brody BA, Kloman AS, Gilles FH. Sequence of central nervous system myelination in human infancy II. patterns of myelination in autopsied infants. *J Neuropathol Exp Neurol* 1988;47:217–234.
30. Mori S, Crain BJ, Chacko VP, van Zijl PCM. Three-dimensional tracking of axonal projections in the brain by magnetic resonance imaging. *Ann Neurol* 1999;45:265–269.
31. Conturo TE, Lori NF, Cull TS, Akbudak E, Snyder AZ, Shimony JS, McKinstry RC, Burton H, Raichle ME. Tracking neuronal fiber pathways in the living human brain. *Proc Natl Acad Sci USA* 1999;96:10422–10427.
32. Cheng Y, Cory DG. Multiple scattering by NMR. *J Am Chem Soc* 1999;121:7935–7936.
33. Tuch DS, Reese TG, Wiegell MR, Wedeen VJ. Diffusion MRI of complex neural architecture. *Neuron* 2003;40:885–895.
34. Zhang J, Richards LJ, Yarowsky P, Huang H, van Zijl PCM, Mori S. Three-dimensional anatomical characterization of the developing mouse brain by diffusion tensor microimaging. *Neuroimage* 2003;20:1639–1648.
35. Stanisz GJ, Szafer A, Wright GA, Henkelman RM. An analytical model of restricted diffusion in bovine optic nerve. *Magn Reson Med* 1997;37:103–111.
36. Sukstanskii AL, Yablonskiy DA, Ackerman JJH. Effects of permeable boundaries on the diffusion-attenuated MR signal: insights from a one-dimensional model. *J Magn Reson* 2004;170:56–66.
37. Chin C-L, Wehrli FW, Hwang SN, Takahashi M, Hackney DB. Biexponential diffusion attenuation in the rat spinal cord: computer simulations based on anatomic images of axonal architecture. *Magn Reson Med* 2002;47:455–460.
38. Cohen Y, Assaf Y. High b-value q-space analyzed diffusion-weighted MRS and MRI in neuronal tissues—a technical review. *NMR Biomed* 2002;15:516–542.
39. Kroenke CD, Bretthorst GL, Inder TE, Neil JJ. Diffusion MR imaging characteristics of the developing primate brain. *NeuroImage* 2005;25:1205–1213.
40. Jones DK, Basser PJ. “Squashing peanuts and smashing pumpkins”: how noise distorts diffusion-weighted MR data. *Magn Reson Med* 2004;52:979–993.
41. Sijbers J, den Dekker AJ. Maximum likelihood estimation of signal amplitude and noise variance from MR data. *Magn Reson Med* 2004;51:586–594.